

BLAEs – I. Resolving the UV-continuum emission in Lyman alpha emitting galaxies between redshift 2 to 3 with gravitational lensing

E. Ritondale,^{1*} A. N. Other,² Third Author^{2,3} and Fourth Author³

¹*Max Planck Institute for Astrophysics, Karl-Schwarzschild-Strasse 1, D-85740 Garching, Germany*

Accepted XXX. Received YYY; in original form ZZZ

ABSTRACT

Lyman-alpha emitters (LAEs) are low-mass, high specific star formation rate galaxies that are thought to be predominantly responsible for the reionisation of the Universe. In spite of their importance, it is extremely difficult to characterise in detail all but the brightest, most massive of these galaxies; this is unsatisfactory, since the faint LAE population is expected to contribute significantly to the reionisation. Here we present a study of a new sample of 20 strongly lensed Ly- α emitting galaxies at $z \sim 2.3$, where we take advantage of the lensing magnification (typically a factor of about 20) to characterise some of the physical properties of low star-formation rate LAEs for the first time.

Key words: gravitational lensing – galaxies: structure

1 INTRODUCTION

Lyman-alpha emitting galaxies (LAEs) represent a population of star-forming systems with very large Ly α equivalent widths and some of the highest specific star-formation rates (sSFR) in the Universe, and these low-mass galaxies are thought to be predominantly responsible for the reionisation of the Universe. However, it is extremely difficult to characterise these galaxies in detail because they are intrinsically very faint. Typical LAE galaxies have strong star-formation, high-ionisations, and are typically low metallicity; these properties, combined with a (mostly) low dust content, allow for the escape of a large fraction of Ly α photons. At redshift $2 < z < 3$, well-studied LAEs are typically at the bright end of this parameter space, being L* galaxies with $M_* \sim 10^9 M_\odot$ and typical SFRs of about 30 to 100 M_\odot/yr (e.g. Erb et al. 2016), and investigations of lower-SFR objects have generally been limited to quantifying the properties of strong optical lines (e.g. Trainor et al. 2015). For example, Hagen et al. (2016) have recently shown that low-SFR LAEs (M_* as low as $10^7 M_\odot$ and $\text{SFR} \sim 1$ to 100 M_\odot/yr , consistent with local-Universe *green pea* LAEs, e.g., Henry et al. 2015) have optical strong line ($\text{H}\alpha$ and $[\text{O III}]$) properties consistent with optically-selected star-forming galaxies of the same masses at $z \sim 2$, but they are unable to directly determine the properties of these galaxies that may

affect the UV escape fraction, including the gas metallicity, density, and kinematics, without additional very large investments in telescope time. Strong gravitational lensing can be used to overcome this limitation, but the difficulty is that most strongly lensed galaxies at $z \sim 2$ are not LAEs, and at present the properties of only three lensed LAEs have been investigated in detail (Christensen et al. 2012; Vanzella et al. 2016). Fortunately, new HST V-band observations of LAE galaxies selected from the BOSS survey have revealed a sample of strongly lensed systems at $\langle z \rangle \sim 2.5$ for which the magnification effect could reveal the detailed structure of these LAEs at scales around 100 pcs. Our subsequent lens modelling shows that the typical lensing magnification of these objects is $\mu \sim 20$ and, after accounting for this magnification, these objects are compact galaxies with SFRs of $\sim 12 M_\odot/\text{yr}$ (i.e., a factor of 3 to 8 lower than previous detailed studies).

2 OBSERVATIONS

The BLAEs sample was observed with the *Hubble Space Telescope* (HST) using the WFC3 camera and the F606W filter ($\lambda_c = 5887 \text{ \AA}$; $\Delta\lambda = 2182 \text{ \AA}$) between 2015 November and 2016 May (GO: 14189; PI: Bolton). In total, twenty one candidate gravitationally lensed Lyman-alpha emitting galaxies from the Shu et al. (2016) sample were observed for about 2600 s each. As their redshifts span from $z \sim 2.1$ to 2.8 and given the transmission curve of the F606W filter, these

* E-mail: elisa@mpa-garching.mpg.de

observations probed the rest-frame ultraviolet emission from young massive stars between 1250 and 2230 Å.

The data were retrieved from the *HST* archive and processed using the *ASTRODRIZZLE* task that is part of the *DRIZZLEPAC* package. Cut-out images for each target are shown in Fig. 1. Out of the twenty one candidates, three turned out not to be strong gravitational lenses with clear multiple images of the same background galaxy (SDSS J0054+2944, SDSS J1116+0915 and SDSS J1516+4954). Also, SDSS J2245+0040 is not included in our final sample because the uncertain nature of the deflector, which appears to be a spiral galaxy, made identifying the emission from the lensed Lyman alpha emitting galaxy challenging without additional colour information. Therefore, the final BLAEs sample used for our analysis contains seventeen gravitationally lensed Lyman-alpha emitting galaxies. The details of the sources in our final sample and the *HST* data that we will use are given in Table 1.

3 MODELLING

The gravitational lens modelling and source reconstruction of each system was performed using a new version of the Bayesian pixelated technique developed by [Vegetti & Koopmans \(2009\)](#). Consider the observed surface brightness distribution \mathbf{d} given by the combination of the lensed image \mathbf{d}_s of an unknown extended background source \mathbf{s} and the surface brightness distribution of the lensing galaxy \mathbf{d}_l . Both \mathbf{d}_s and \mathbf{s} are vectors representing the surface brightness distribution on a set of pixels, on the lens plane and source plane respectively. The grid on the lens plane is defined by the native CCD pixilation of the data, while the grid on the source plane is defined by a magnification-adaptive Delaunay tessellation (see [Vegetti & Koopmans 2009](#), for more details). This provides a pixelated surface brightness distribution for the reconstructed source that is free from any parameterised assumptions, such as Sersic or Gaussian light profiles, that may not fully account for the clumpy nature of the rest-frame ultraviolet emission from the BLAEs sources. The positions of the pixels are related between the two planes by the lensing equation via the projected gravitational potential $\psi(x, \boldsymbol{\eta})$ of the lensing galaxy, defined by the unknown parameters $\boldsymbol{\eta}$. Taking advantage of the fact that gravitational lensing conserves surface brightness and taking into account for the observational noise \mathbf{n} , \mathbf{d} and \mathbf{s} can be related to each other via a set of linear equations,

$$[\mathbf{B}\mathbf{L}(x, \boldsymbol{\eta}) + \lambda \mathbf{R} \mid \mathbf{B}\mathbf{I}(x, \boldsymbol{\eta}_l) \mid \mathbf{1}] \begin{pmatrix} \mathbf{s} \\ I_0 \\ C \end{pmatrix} = \begin{pmatrix} \mathbf{d}_s \\ \mathbf{d}_l \end{pmatrix}. \quad (1)$$

Here \mathbf{B} is the blurring operator that expresses the effect of the point spread function. \mathbf{R} and λ are respectively the form and unknown level of the source surface brightness distribution regularization and are essentially a form of prior on the level of smoothness of the background galaxy. C is a constant pedestal, expressing the sky background. $\mathbf{I}(x, \boldsymbol{\eta}_l)$ is the surface brightness distribution of the foreground gravitational lens, it is simultaneously modelled with the mass distribution and is parametrised using elliptical Sersic profiles of total normalization I_0 , effective radius R_e , Sersic index n

and axis ratio b :

$$I(\mathbf{x}) = I_0 \exp \left[\left(-bn \left(\frac{r}{R_e} \right)^{1/n} - 1.0 \right) \right]. \quad (2)$$

We refer to the Sersic parameters collectively as $\boldsymbol{\eta}_l$. \mathbf{L} is the lensing operators and is related via the lens equations to the lens mass distribution. The latter is parametrized with an elliptical power-law profile of dimensionless surface mass density κ given by

$$\kappa(x, y) = \frac{\kappa_0 \left(2 - \frac{\gamma}{2} \right) q^{\gamma-3/2}}{2 \left(q^2 (x^2 + r_c^2) + y^2 \right)^{(\gamma-1)/2}}, \quad (3)$$

where κ_0 is the surface mass density normalization, q is the axial ratio of the elliptical mass distribution, γ is the radial slope of the mass density profile and r_c is the core-radius. In addition, the position angle of the elliptical mass distribution (θ), and the shear strength (Γ) and positional angle (Γ_θ) as also solved for. We refer to the mass density parameters collectively as $\boldsymbol{\eta}$. The dimensionless surface mass density and the Einstein radius (R_{ein}) are related to each other via,

$$R_{\text{ein}} = \left(\frac{\kappa_0 \left(2 - \frac{\gamma}{2} \right) q^{(\gamma-2)/2}}{3 - \gamma} \right)^{1/(\gamma-1)}. \quad (4)$$

The modelling procedure is performed in two steps: first we masked out the emission from the lens galaxy and, given the lensed surface brightness distribution \mathbf{d} , we optimize for the lens mass parameters $\boldsymbol{\eta} = \{\kappa_0, \theta, q, x, y, \gamma, \Gamma, \Gamma_\theta\}$ and the source regularisation level by maximising the posterior probability density,

$$P(\lambda_s, \boldsymbol{\eta} \mid \mathbf{d}, \mathbf{R}_s) = \frac{P(\mathbf{d} \mid \lambda_s, \boldsymbol{\eta}, \mathbf{R}_s) P(\lambda_s, \boldsymbol{\eta})}{P(\mathbf{d} \mid \mathbf{R}_s)}. \quad (5)$$

At each step of this optimization, the corresponding most probable source \mathbf{s} is obtained by maximising the probability density distribution,

$$P(\mathbf{s} \mid \mathbf{d}, \lambda_s, \boldsymbol{\eta}, \mathbf{R}_s) = \frac{P(\mathbf{d} \mid \mathbf{s}, \boldsymbol{\eta}) P(\mathbf{s} \mid \lambda_s, \mathbf{R}_s)}{P(\mathbf{d} \mid \lambda_s, \boldsymbol{\eta}, \mathbf{R}_s)}. \quad (6)$$

Then, using this as a starting point, we parametrise the surface brightness distribution of the lens galaxy as a sum of multiple elliptical Sersic profiles, and optimise for the corresponding parameters, $\boldsymbol{\eta}_l = \{I_0, R_e, n, b, \theta\}$ together with the background source surface brightness distribution. In the third and last step, we optimise simultaneously for the mass and the light distribution of the deflector and the source regularisation level.

4 RESULTS

5 DISCUSSION

REFERENCES

- Shu Y., et al., 2016, preprint, ([arXiv:1604.01842](#))
 Vegetti S., Koopmans L. V. E., 2009, *MNRAS*, **392**, 945
 Vegetti S., Koopmans L. V. E., Auger M. W., Treu T., Bolton A. S., 2014, *MNRAS*, **442**, 2017

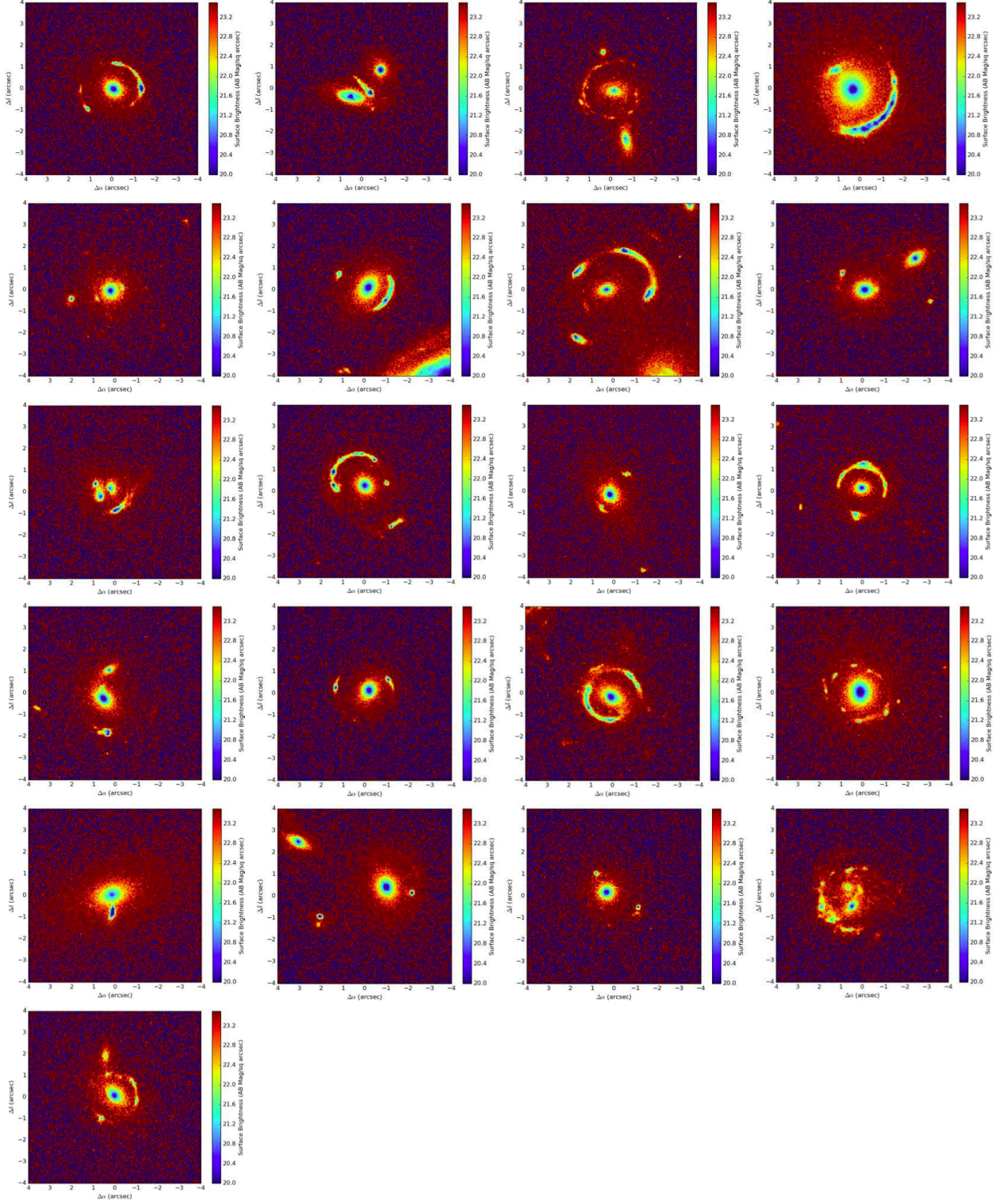


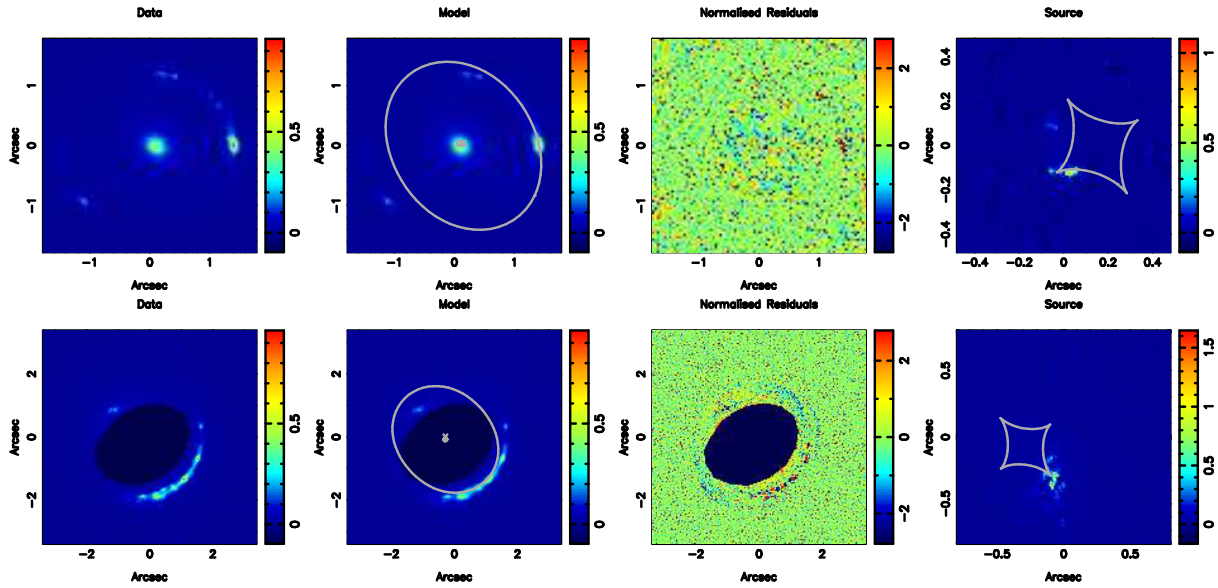
Figure 1. The WFC3 F606W imaging with the *HST* of each candidate gravitational lens. The cut-outs are 8×8 arcsec² in area, and the surface brightness scale is in AB magnitudes arcsec⁻². **Names and redshifts to be added.**

Table 1. Details of the BLAEs sample used for our analysis and the derived gravitational lens mass models.

Name (SDSS)	z_{lens}	z_{src}	$\lambda_{\text{rest}} [\text{\AA}]$	Exp. Time [s]	$R_{\text{ein}} [\text{arcsec}]$
J0029 + 2544	0.587	2.450	1706	2504	1.330
J0113 + 0250	0.623	2.609	1631	2484	1.225
					0.070
					0.173
J0201 + 3228	0.396	2.821	1540	2520	
J0237 – 0641	0.486	2.249	1812	2488	0.536
J0742 + 3341	0.494	2.363	1751	2520	1.208
J0755 + 3445	0.722	2.634	1620	2520	
J0856 + 2010	0.507	2.233	1821	2496	0.745
J0918 + 4518	0.524	2.344	1761	2624	
J0918 + 5104	0.581	2.403	1730	2676	
J1110 + 2808	0.607	2.399	1732	2504	0.985
J1110 + 3649	0.733	2.502	1682	2540	1.145
J1141 + 2216	0.586	2.762	1565	2496	1.281
J1201 + 4743	0.563	2.126	1883	2624	1.186
J1226 + 5457	0.498	2.732	1578	2676	
J1529 + 4015	0.531	2.792	1553	2580	
J2228 + 1205	0.530	2.832	1536	2492	1.270
J2342 – 0120	0.527	2.265	1803	2484	1.088

Table 2. Add caption here. This table should contain the best parameters for the sersic models

Name (SDSS)	n_{Ser}
-------------	------------------

**Figure 2.** From top to bottom: best models for the lens gravitational systems From left to right: input data, reconstructed model, normalised image residuals and reconstructed source.

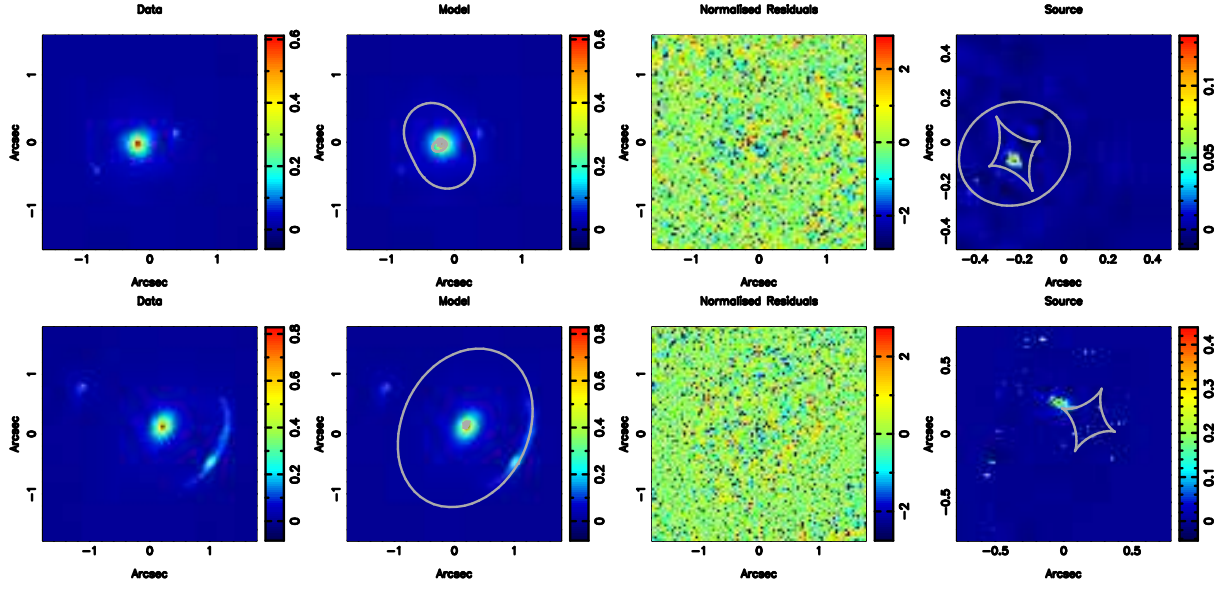


Figure 3. Same as Fig. 2 for the gravitational lens systems

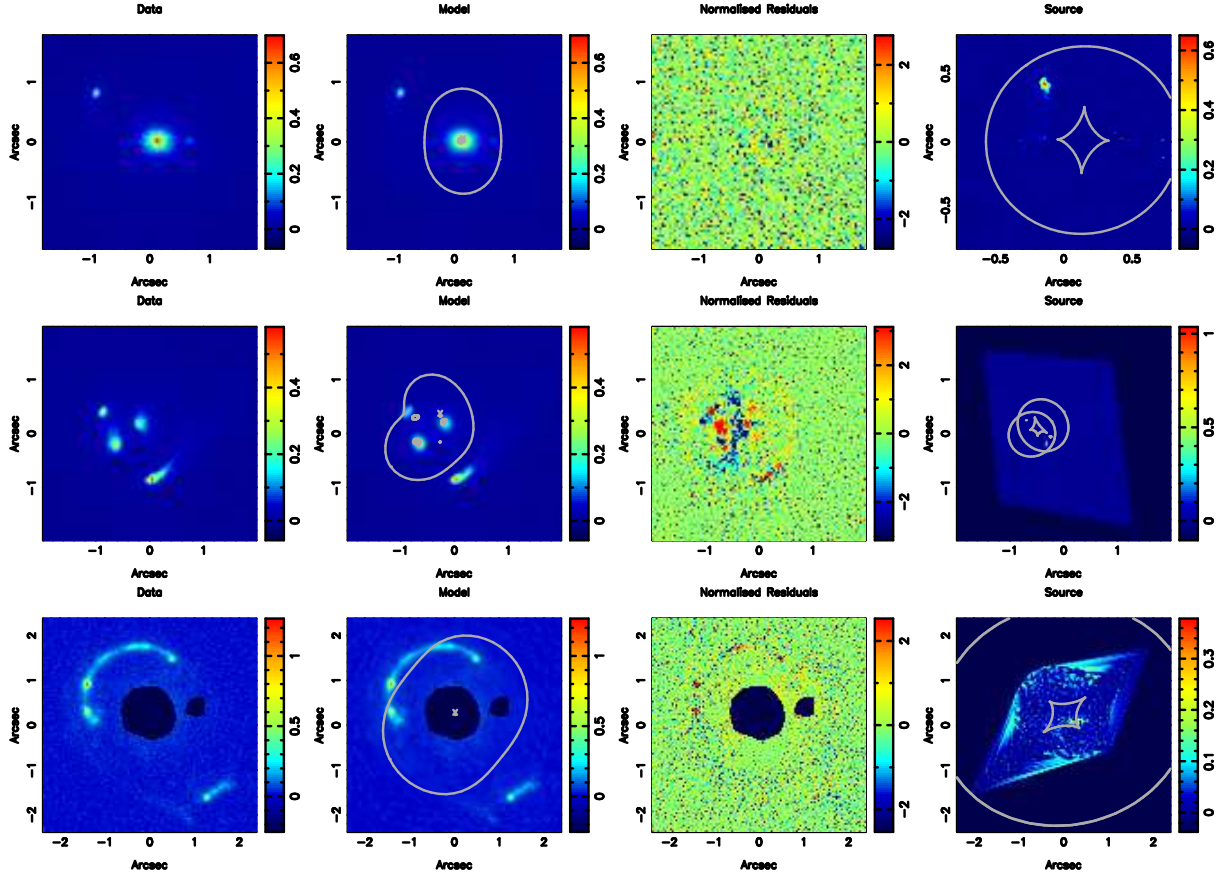


Figure 4. Same as Fig. 2 for the gravitational lens systems

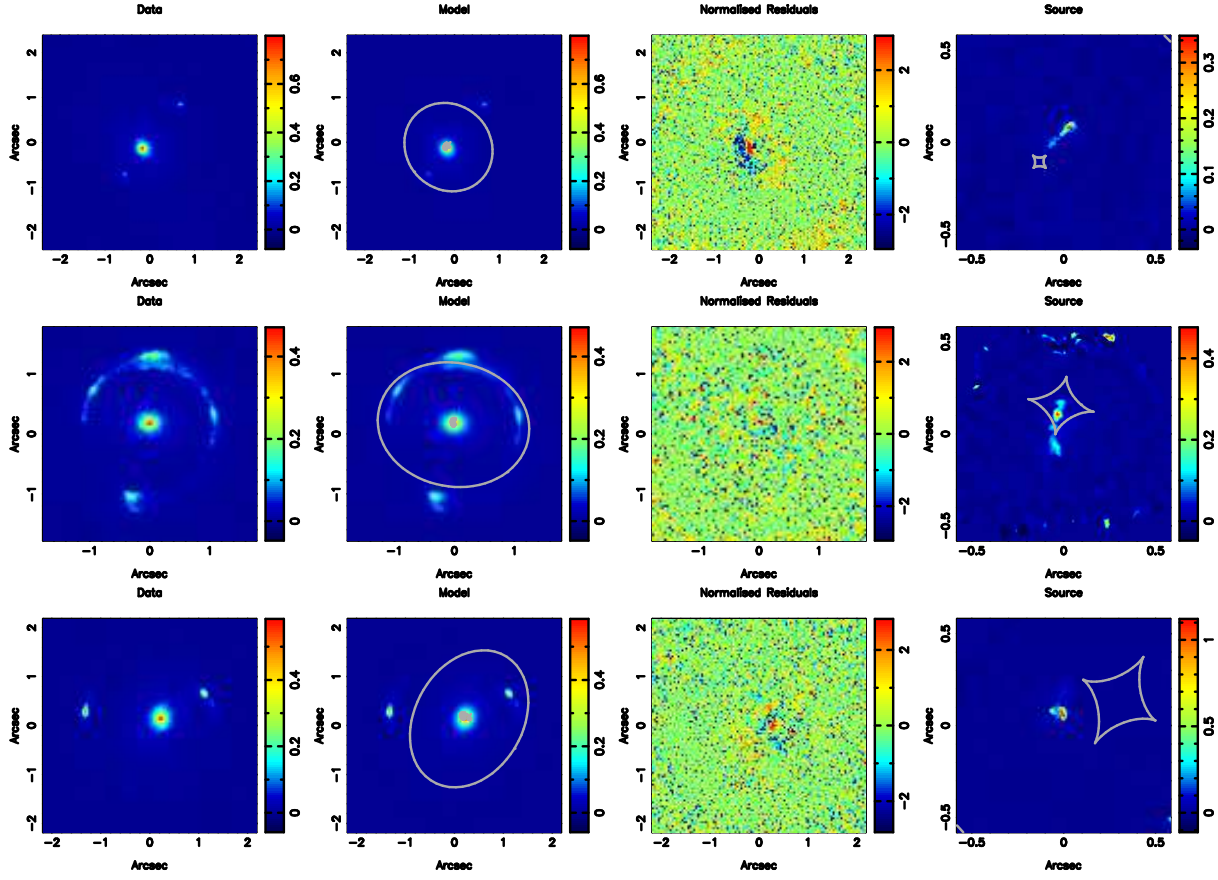


Figure 5. Same as Fig. 2 for the gravitational lens systems

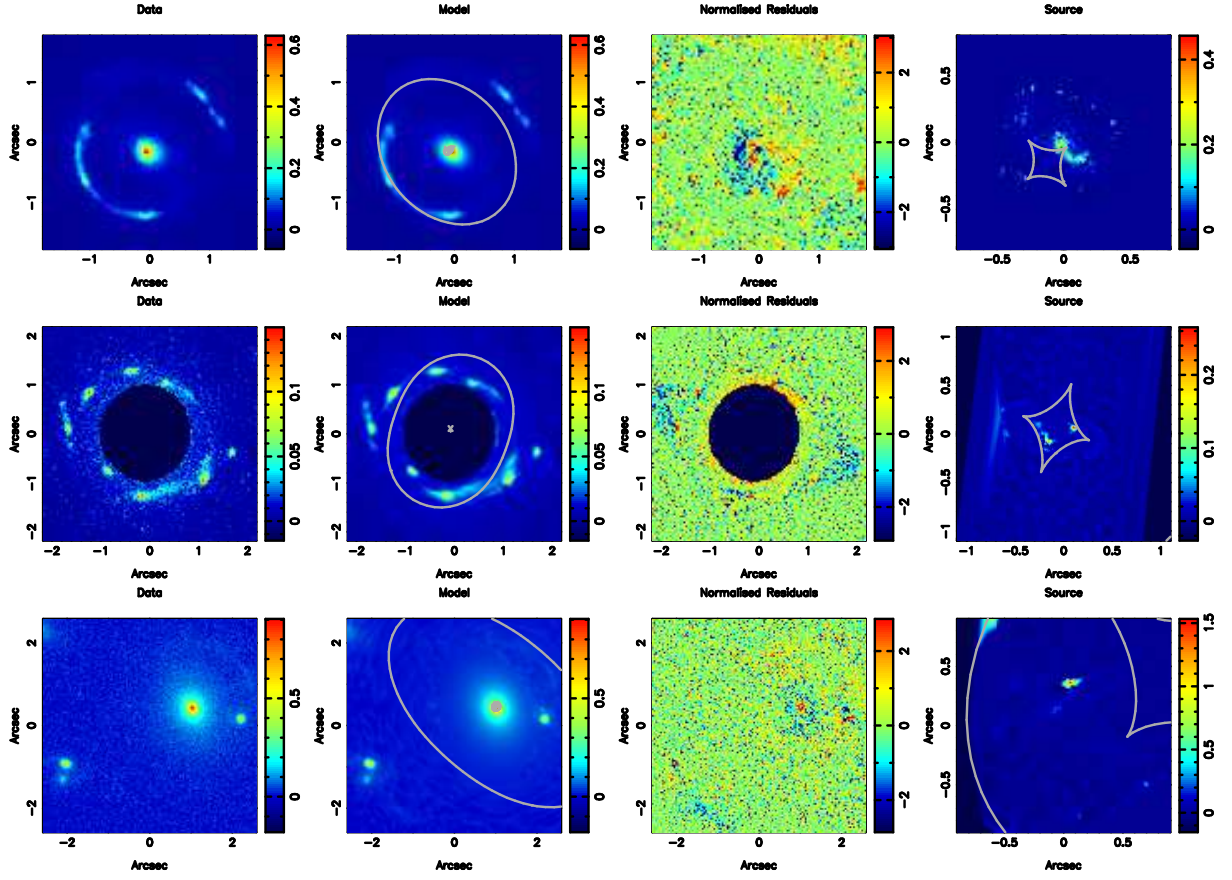


Figure 6. Same as Fig. 2 for the gravitational lens systems

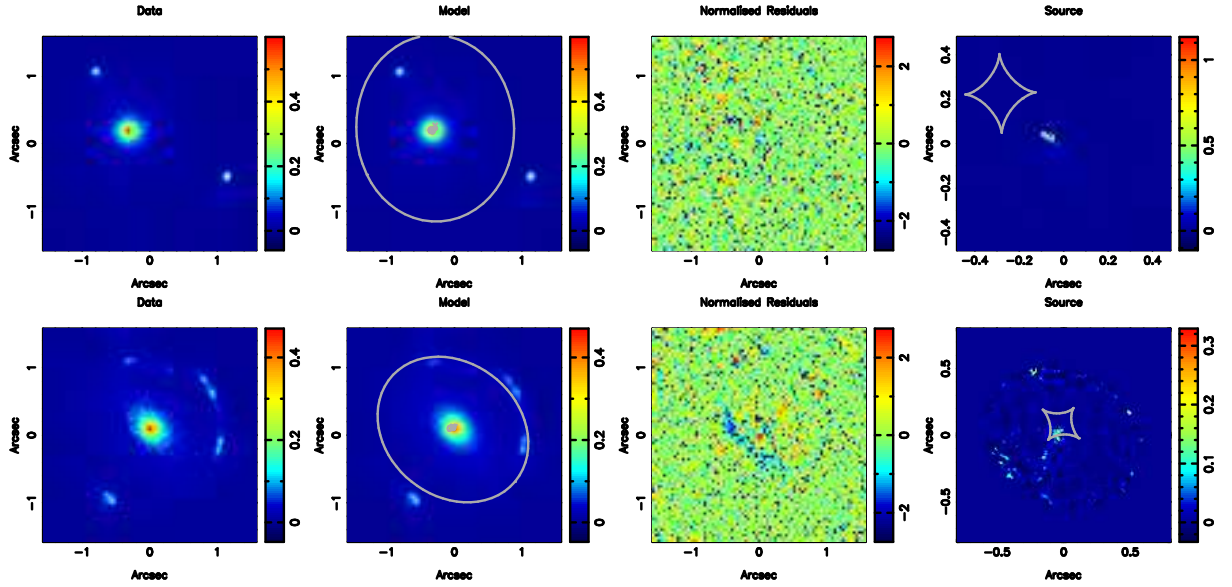


Figure 7. Same as Fig. 2 for the gravitational lens systems